Title : Towards centimeter precision SAR-RFID localization

Authors : Arthur Charléty, Morgane Magnier, Mathieu Le Breton, Eric Larose, Laurent Baillet, Ludovic Moreau

Contacts : arthur.charlety@univ-grenbole-alpes.fr

Paper sent for peer-review to : ISPRS Journal of Photogrammetry and Remote Sensing

Towards centimeter precision SAR-RFID localization

Highlights

Towards centimeter precision SAR-RFID localization

- SAR-RFID localization is demonstrated with centimeter accuracy and real-time acquisition
- The sources of error of SAR-RFID localization are reviewed in an operationnal manner
- Localization under vegetation and snow cover is demonstrated
- Markov-Chain Monte-Carlo algorithm enhance the localization results
- A comparison of antenna tracking methods shows Post-Processed Kinematics yields better results for outdoor tracking

Towards centimeter precision SAR-RFID localization

Abstract

Radio-Frequency Identification (RFID) shows great potential for earth-sciences applications, notably for landslide surface monitoring at a high spatio-temporal resolution with long-term robustness to meteorological events (rain, fog, snow). The ability to localize RFID tags using Unmanned Aerial Vehicles (UAV) in a Synthetic Aperture Radar (SAR) approach, would offer new possibilites for monitoring inaccessible terrains, even under vegetation and snow. To that end, an onboard measurement system was built that allows Global Positionning (GPS) tracking of an RFID reader antenna, in order to perform real-time SAR measurement acquisition of RFID tags on the ground. Three antenna tracking methods were compared. In addition, Markov-Chain Monte-Carlo (MCMC) optimization was used to estimate tag position and characterize the solution, even in non-convex cost function scenarios. Two cost functions were compared, based on different RFID-phase processing approaches. Real-time SAR-RFID localization yielded a centimeter accuracy in the horizontal plane, with lower resolution in the vertical direction. The Post-Processed Kinematics algorithm proved to best fit antenna tracking. The unwrapped-phase based cost function provided more convex solutions, at the cost of a lower accuracy compared to the complex-phase cost function. MCMC proved to be computationally efficient in SAR-RFID optimization, with enhanced results concerning the shape and orientation of the main localization errors.

Keywords: RFID, UAV, SAR, Synthetic Aperture Radar, Unmanned Aerial Vehicle, Radio Frequency Identification, Remote Sensing, localization, Markov Chain Monte Carlo, vegetation, snow, landslide monitoring.

1. Introduction

In the recent years, the use of Unmanned Aerial Vehicle (UAV) as a means of remote sensing has been a growing research topic [1, 2]. In Earth Sciences and Environmental Remote Sensing, UAVs provide a relatively cheap solution to investigate unreachable or dangerous places for humans [3, 4]. Compared to satellite-based remote sensing, UAV's allow for a more local and flexible investigation, especially in terms of acquisition frequency. Compared to heavier local devices (fixed Lidar, total station, etc), they represent a lighter solution free to investigate both wide areas and specific objects. With the Internet-of-Things (IoT) paradigm, new sensing systems are appearing in which the role of UAVs is of importance, notably in telecommunication [5] and agriculture [6]. Radio-Frequency Identification (RFID), which is an important domain in IoT [7], has acquired rising interest in the Earth Science community [8] for a variety of applications such as pebble tracking, soil moisture sensing, snow depth estimation [9], or landslide displacement monitoring. The combination of UAV and RFID technologies provides great possibilities in the domains of logistics and retail [10], but also in environmental sensing [11, 12]

and notably ground surface displacement sparse monitoring [13]. Landslides are complex natural hazards, under investigation since decades. Monitoring is essential both to study landslide dynamics and to create early warning system. Surface displacement is commonly monitored and predicted using a wide variety of technical devices, in order to warn the affected communities when necessary [14]. Aerial remote sensing solutions include Interferometric Synthetic Aperture Radar (InSAR) and airborne imagery. Stable in-situ methods rely on total stations, Lidar devices, GNSS or extensometer, and recently RFID landslide monitoring was demonstrated [15] and improved [16, 17] with a system of fixed antennas in both 1D and 2D localization schemes [8, 18]. Most methods suffer from specific outdoor conditions, such as steep slopes, rain and fog, snow, vegetation or wandering animals. The above-cited approaches can hardly measure accurate displacements under vegetated cover, even less in the case of snow as its surface movement (snow creep) does not match ground deformation. In this context, RFID shows interesting features that allow measurements without a free line-of-sight between readers and tags, with a manageable sensitivity to vegetation and snow [19]. Although the interactions between RFID systems and snow or vegetation have been partly studied [15, 9], tag localization in these media has not yet been demonstrated. As of now, RFID measurement systems installed on landslides have always been fixed stations [8, 18]. We foresee the development of UAV-RFID localization as a promising method, that could greatly enhance the size of RFID-monitored sites, ensuring a vegetation- and snow-ready measurement technique [20]. This paper proposes to investigate the intricate challenges of UAV-RFID landslide monitoring, and monitoring under vegetation or snow cover : can we monitor surface displacement through snow and vegetation using UAV-RFID, and with which accuracy ? First, we introduce the SAR-RFID localization approaches and review the various localisation errors and the corresponding litterature (Sec. 2). The performed experiments are then described in the Materials and Methods (Sec. 3). Next, specific aspects concerning RFID data inversion are covered (Sec. 4). Last, the localization results are presented and discussed (Sec. 5).

2. Operational review for outdoor localization

UAV-aided RFID localization using phase-of-arrival measurement, is a challenge that puts several technologies and methodologies into play. It is a complex problem that implies many sources of error and offers a variety of choices at every step of the workflow. Table 1 proposes a summary of all steps in the measurement chain, to the best of our knowledge, and the corresponding literature works. This table was constructed in an operational perspective, in order to help decipher and reduce individual error sources.

First the localization of the drone and the antenna attached to it, can be performed in multiple ways (”Reader Positioning” section in Table 1). Using a single GNSS receiver, Precise Point Positionning (PPP) can provide centimeter accuracy after post-processing of GNSS data [21]. This method often requires dual-frequency measurement and is best suited for immobile antenna positioning [22]. Differential methods using base and rover GNSS receivers, such a Real Time Kinematic (RTK) or Post Processed Kinematics (PPK), only require mono-frequency measurements to reach centimeter accuracy. The latter proved to be more accurate than RTK, as it allows better correction from GNSS satellites data [23]. It also provides more stable solutions than RTK. Nonetheless the loss of a fixed-integer position can occur, leading to the absence of usable data points. To prevent this, Suzuki *et al.* [24] used the redundancy of multiple GNSS receivers mounted on the same drone. Another solution would be to track the UAV-antenna using a total station [25]. Although this would yield the best accuracy (it is used as a reference compared to

GNSS), it would also cancel many advantages of the approach : heavy ground-based devices, and need for line-of-sight.

When performing measurements with a flying antenna, the relative position of the GNSS rover with respect to the antenna position, both rotating around the UAV center of mass, can vary because of tilt [26] : the so-called "lever-arm effect". This effect is even accentuated in outdoor scenarios, and when the drone flies at high speed or follows an erratic trajectory because of the wind. The use of an embedded inertial measurement unit (IMU) for correction can therefore be necessary. In the present scenario, all experiments where performed at low velocity (a few cm/s at most) on a stable support, so that no inertial correction was required. See "Reader Antenna positioning" in Table 1.

Variations in the phase center position are also prone to appear ("Phase meas." in Table 1), notably with varying reader angle as studied in [27] or due to a metallic surrounding. In extreme angle geometries, this can lead to a 1.2rad phase offset (3 cm with the present UHF devices). The presence of the metallic drone structure is generally accounted for, by setting the phase center 10 cm above the antenna's center of mass [28]. The combination with antenna tracking errors (drone position + tilt) then produces non-negligible uncertainties between the real phase center and the tracked one.

In every RFID-SAR scenario, the shape of the trajectory has a notable impact on the localization performance. A general rule states that the longer the trajectory in one direction, the better the localization accuracy. The shape of the trajectory can generate secondary peaks in the inversion process, as studied elsewhere using simulation [29]. In scenarios where the antenna overlooks tags placed on the ground, the trajectory should have maximal vertical and horizontal extension. Measurements from multiple antennas are also used to increase the size of the SAR without actually increasing the antenna trajectory[30].The spatial sampling frequency should follow Shanon's criterion, which imposes a limit on the flight speed in the case of real-time measurements. During the measurement process, usual phase measurement errors are expected, with a notable relationship to RSSI values [15]. Moreover, in the case of rough terrain or presence of water (humid vegetation, snow, soil moisture), multipath interference may generate measurement biases that can hardly be simulated nor canceled.

Another critical aspect of this multi-measurement setup is the time synchronization of RFID, GNSS and potentially IMU data. At a flying speed of 1 m/s a time delay of 10 ms can lead to a 1 cm space offset between UAV position and corresponding RFID measurement.To overcome this issue, trigger events have been used for initial synchronization [28]. Added to this difficulty, is the fact that GPS measurements are under-sampled compared to RFID.

Once the measurement is performed, the inversion problem poses yet another set of issues ("Inversion problem" in Table 1). RFID phase data is usually taken in its complex form and the cost function is defined by the correlation between measured and synthetic vector [28]. Other methods rely on segmented phase unwrapping, which tends to reduce the localization ambiguity [31, 27]. Lastly, the optimization algorithm is a crucial choice in terms of computational cost. A grid-search approach can be used for exhaustive characterization [29], but in real cases other methods have been explored : Particle Swarm Optimization (PSO) was lately used for complex-phase and non-convex cost functions [30], and simpler gradient methods were applied to unwrapped-phase convex cases [31]. In general it is more efficient to exploit all available observables such as RSSI and phase, in order to reduce the search window and then perform a more costly inversion [27].

Error source	Comment / solution	Error estimate	Literature
Reader Positioning			
GNSS processing	PPK/RTK/PPP, depends mostly on hardware and technical needs.	1-5 cm	[32, 23, 24], this paper
Loss of GNSS ambiguity resolution	Related to sky view / multipath environment. IMU can help.	Data loss	[24, 33]
Sky view	DOP, satellite clock errors. Implies a time-varying bias.	1-10 cm	[34, 35]
Reader Antenna Positioning			
Lever-arm effect	Requires IMU.	1-10 cm	[26, 36, 37, 38, 39]
Time sync between GPS and RFID measurement	Trigger event, or NTP sync. Need to handle subsampling interpolations (potentially with IMU).		[28, 40, 41], this paper
GPS/RFID subsampling	Interpolation using IMU or other methods.		[42]
Phase meas.			
Antenna phase center variation	Angle (antenna directivity) and environment dependent.	1-10 cm	[27, 28]
Random phase error	Depends on antenna and signal strength.	1 cm	[15, 18]
Propagation phase error	Multi-path interference, media-dependent delay.	1-20 cm	[18, 43, 44, 45], this paper
Doppler phase shift	Depends on UAV velocity.		[46, 47]
Inversion problem			
Shape of trajectory	Secondary peaks could appear. SAR length should be maximized in all directions.		[29, 30]
Density of points	Shanon criterion should be respected, even with trajectories distant in time.	1-10 cm	[29, 48]
Choice of cost function	Wrapped/unwrapped phase, differential, RSSI.		[28, 30, 49, 50, 31], this paper
Inversion algorithm	Computation time, accuracy, precision estimation.		[29, 30, 50], this paper

Table 1: Errors sources for UAV-RFID localization.

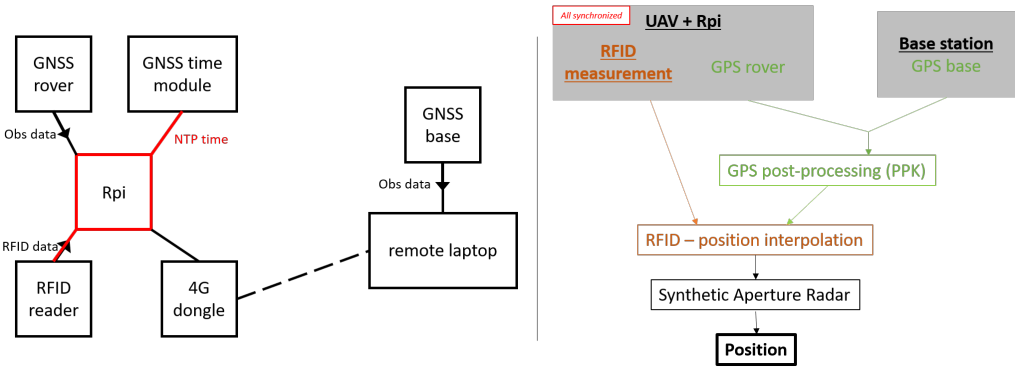

Figure 1: (Left) Schematic of the SAR embedded measurement system. (Right) Workflow for data processing, from raw measurement to SAR inversion.

3. Materials, methods and workflow

3.1. Experimental test structure, embedded system

An experimental setup was built to simulate the embedded system that would fly on a real drone, with all devices mounted on a fiber glass structure (see Figure 2). This structure, inspired by [51], allowed for a 1D-SAR trajectory of length 1.6 m without actually flying a UAV.

The GNSS signal was provided by a receiver, connected to a local base with short baseline (<10 m). RFID measurements were performed with a reader connected to a circular polarized RFID antenna, using a carrier frequency of 867 MHz and at a sampling frequency of 20 Hz. Internet and wireless connection was provided by a 4G+ modem. Time synchronization was performed by using a supplementary GNSS dongle [41] through a local NTP server to which the RFID reader was synchronized. This way a millisecond-order delay was ensured between all measurements. All the devices were connected to a Raspberry Pi (Rpi), that launched and stored the various measurements. This measurement system was then moved on a rail structure made of fiber glass, guiding the system on a 1D trajectory. The height and orientation of the structure varied in the different experiments. Lastly, a mini-prism was mounted on the system to perform tacheometry reference measurements [52]. Figure 1 presents a general scheme summarizing the measurement setup, as well as the construction of the SAR data.

3.2. Processing data to produce the SAR

The Synthetic Aperture Radar is a composite vector, combining both reader position and corresponding phase measurement. This section describes the construction of this SAR vector from raw measurements.

First we will discuss the SAR trajectory tracking. In this study PPK and RTK were used for reader tracking, along with tacheometry for reference measurement. For PPK, the raw observation files measured from the base and rover were post-processed using RTKLib [53] to obtain a 5Hz-sampled position series. For RTK, the pyUBX [54] python module was used. In both cases, when the ambiguity resolution was lost (leading to a floating point solution), the data was discarded.

The SAR vector consists of both 3D position and 1D phase measurements, in a $4 \times N_r$ shape, where N_r is the total number of readings. Due to different sampling frequencies an interpolation

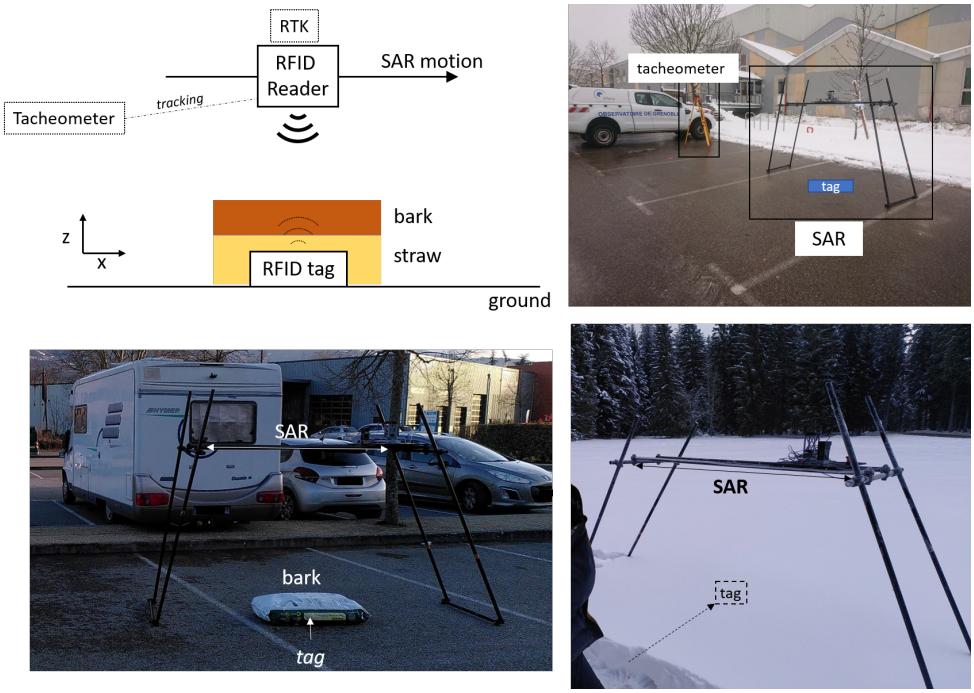

Figure 2: Summary of the 1D experiments. (Top left) Schematic of the typical 1D measurements. (Top Right) Experiment in air. (Bottom Left) Vegetation experiment. (Bottom Right) Snow experiment.

of the antenna position is required. A spline interpolation was applied for continuous measurements that respect the Shannon criteria, although IMU-based interpolation could yield better results. When the criteria was not met, no interpolation was performed. In real-time acquisition scenarios, i.e. when the antenna position changes between every RFID measurement, high acceleration periods were discarded because the tilt, vibrations or elastic deformation could disrupt the geometrical relationships between the different system devices.

3.3. Step-by-step 1D-SAR experiments

The following experiments were performed using the fiber glass structure fixed on the ground (see Figure 2). During experiments the system was moved manually step by step, with a 10 s step measurement duration. This allowed for a stable configuration at each point. The spatial increment between measurements was 3 cm. Pointwise tacheometer references were taken using a total station and the mini-prism. The 1D-localization experiments were performed using the fiber glass structure, in a variety of propagation media.

- Vegetation : Two different vegetation types were tested : blocks of hay (30 cm thick) and layers of bark (20 cm thick), with different moisture contents. The materials were superimposed in various geometries over the tags before the SAR measurement, as represented in Figure 2. The moisture content was estimated by drying the material and weighing it (see Table 3).

- Snow : In freezing conditions, a tag was placed below a 28 cm thick homogeneous dry snow layer, with an average density of 0.54 kg/L. The homogeneity of the snow was verified with snow density measurements at various depths, and the snow temperature profile was measured as well. This confirmed dry snow conditions (negative temperature on the whole profile). The structure was placed to perform 1D measurements both with and without the snow layer.

3.4. Real-time 3D-SAR experiments

A set of experiments was performed with continuous movement and real-time sampling. The fiber-glass structure was handheld to perform 3D trajectories, during synchronized measurement from GNSS and RFID. The antenna velocity was low (a few cm/s) and kept a steady orientation, as was confirmed by inertial measurements. The real-time measurement campaigns were performed in clear sky conditions.

4. From SAR to tag position : inversion methods

In this section, the methods used to estimate the tag position from the SAR tracking and phase measurements are discussed. First, two cost functions are compared ; then a heuristic method is proposed to reduce the inversion search space ; finally, we discuss the importance of the vertical antenna tracking error on the final localization result.

4.1. Choice of cost function

In this section, two different cost functions are presented for SAR inversion in order to compare them : complex phasor correlation and guided unwrapping.

C_1 : Complex phasor correlation. Most phase-based SAR-RFID localization works [28] use the following scheme in order to localize an RFID tag with a moving antenna. Let s_i be the complex phase value measured at time i. In this work we do not consider the signal amplitude, as the localization only exploits phase values. Each phase measurement ϕ can be expessed as :

$$\phi_i(p_{ant}, p_{tag}) = -4\pi r_i/\lambda + \phi_0 + \phi_{bias} \tag{1}$$

Where λ is the carrier wavelength, r_i is the distance between antenna and tag phase center positions p_{ant} and p_{tag}, ϕ_0 is an unknown phase offset due to phase propagation in the reader, cable and reading antenna, and ϕ_{bias} is a bias due to multipath or antenna phase center variation. Note that ϕ_0 is supposed constant. Also, ϕ_{bias} is not modeled in this work : it is only a second order quantity. We will neglect ϕ_{bias} in the following, but will nonetheless discuss it later. The complex phasor s_i is defined as follows :

$$s_i = e^{-j\phi_i} = e^{-j(-4\pi r_i/\lambda + \phi_0)} \tag{2}$$

In the following we only consider the phase variation and not the absolute phase value, in order to remove the constant ϕ_0. Usually this is done by subtracting the first measurement :

$$\Delta s_i = \frac{s_i}{s_0} \tag{3}$$

and reducing the measurement vector $\mathbf{y}$ to a normalized phasor sequence :

$$\mathbf{y}(p_{ant}, p_{tag}) = [1,\ \Delta s_1\ ...\ \Delta s_n]$$

Inversion is performed by producing a synthetic measurement vector $\mathbf{a}$ based on a hypothetical tag position p'_{tag} and the estimated antenna trajectory :

$$\mathbf{a}(p_{ant}, p'_{tag}) = [1,\ \Delta s'_1\ ...\ \Delta s'_n]$$

The best match between the measured and synthetic vectors is then found through the normalized correlation product :

$$C_1(p'_{tag}) = \frac{|\mathbf{a}^H \mathbf{y}|}{||\mathbf{a}||\ ||\mathbf{y}||}$$

With H the Hermitian operator. The argument of maximum value for C_1 corresponds to the highest likelihood for tag position.

C_2 : Guided phase unwrapping. Phase unwrapping is a crucial aspect of phase-based RFID localization, usually associated to cost-function convexity and more constrained localization solutions. The complex trajectory of outdoor UAV flights and on-board data acquisition, add to the difficulty of ad-hoc phase unwrapping. Additionally, rough terrain and humidity generate unpredictable multipath interference, and loss of data points can lead to phase decoherence.

We propose a simple algorithm derived from fixed-antenna RFID monitoring [17] in order to perform unwrapping based on a model. To keep track of phase coherence, we utilize the synthetic unwrapped-phase vector for every test point $\mathbf{b}$ built through Eq.1 as a reference for unwrapping the measured wrapped phases $\mathbf{y}$:

$$\mathbf{y}_g = U(\mathbf{y} - \mathbf{b}) + \mathbf{b} \tag{4}$$

With U an unwrapping operator as discussed in [27, 55], the choice of which is not the subject of this work. In the present case we used the complex smoothing unwrapping approach, presented in [17]. Note that the knowledge of ϕ_0 remains unnecessary as we can still normalize both vectors to the first measurement. The guided output $\mathbf{y}_g$ is thus unwrapped to correspond to the test point phase series $\mathbf{b}$, especially after long data gaps. The proposed cost function is the same as C_1, in order to obtain comparable cost functions.

$$C_2(p'_{tag}) = \frac{|\mathbf{b}^H \mathbf{y}_g|}{||\mathbf{b}||\ ||\mathbf{y}_g||}$$

We have herein presented two cost functions for SAR inversion. The next two sections will discuss the inversion approach, first reducing the search space, then using MCMC to characterize the cost function.

4.2. Pre-localization method

In order to reduce computational cost, it is necessary to have a relatively small search zone. Additionally it is important to use a robust convergence algorithm, to prevent incorrect localization results due to secondary peaks. Final inversion is generally performed using only phase measurements, but pre-localization can be performed using more classical RSSI-based algorithms [56, 57]. Even though the latter show accuracy on the order of $0.5 - 1$m, it reduces the search window and the computational cost in a cubic manner. In this work we use the RSSI maximum as the horizontal center of the search space, which is a cube of variable size depending on the experiment.

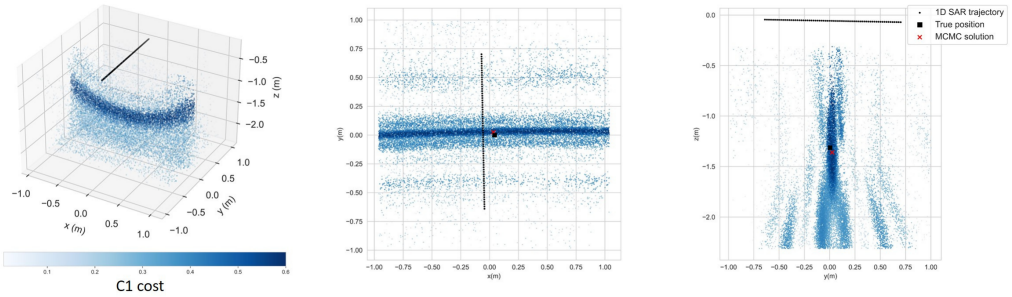

Figure 3: Qualitative results for the localization of a tag using a 1D SAR and tacheometry for antenna tracking. (Left) 3D view of the MCMC distribution (180 000 points out of 800 000 candidates). (Middle) xOy and yOz (right) projections of the MCMC distribution. The colors represent the corresponding cost using C1. The true and estimated position are shown as crosses.

4.3. Inversion algorithm

In this section, the choice of the optimization method is discussed, which is an important matter as well. Firstly because the cost function is generally non-convex, and gradient-based algorithms do not converge towards a stable solution. Secondly because an exhaustive search (gridsearch for instance) implies a high computational cost, especially in the case of a 3D search in a meter-wide window. For both research purposes and real-world applications, using an efficient algorithm to find the tag location is thus crucial.
In a real-world outdoors scenario, with uncertain antenna elevation due to rough terrain, and unstable trajectories due to wind and obstacles, typical inversion methods do not provide stable minima. As was studied elsewhere [29], the shape of the cost function greatly depends on the SAR trajectory, with secondary peaks often appearing.

This paper proposes to use a Markov-Chain Monte Carlo (MCMC) optimization, which is suited for global optimum research of non-convex cost-functions [58]. Moreover MCMC constructs a covariance matrix in the parameter space, providing useful information about the main directions of error. This paper will not go into detail concerning this method, only stating that MCMC builds a Markov Chain that approximates the probability distribution of a given function, here C_1 or C_2. One classical way of building this Markov Chain is the Metropolis-Hastings algorithm, which we use here. In this algorithm, the Markov-Chain possesses the ergodic property. This ensures that, after a burn-in phase, it will reach a stationary state where each position will be visited a number of times proportional to its probability, thus approximating the probability density function of the parameters. The general approach is inspired from [59, 60]. To speed up the burn-in phase of the Metropolis-Hastings algorithm, we perform simulated annealing (SA) to find a starting position close to the global optimum [61], while simultaneously providing an estimate of the variance of the measurement errors [59]. Simulated annealing is also an MCMC method and follows a similar procedure to the Metropolis–Hastings algorithm. However, rather than approximating the probability density function of the parameters, it aims at converging to the global optimum by progressively decreasing the probability of accepting worse solutions. From the simulated annealing, the best output and the estimated variance are used as input to a classical Metropolis-Hastings exploration of the search space.
Typical computation times in this paper are in the order of 1×10^5 iterations for SA and 8×10^5 for MCMC. As a quick comparison, a gridsearch algorithm would require 6.4×10^7 computations

to reach a 0.5cm accuracy in a search cube of 2m side.

4.4. Sensibility to antenna position uncertainty

In the SAR-RFID scenario, there is a doubled negative effect from the system sensitivity in the vertical direction. It is widely documented that GPS solutions show a higher uncertainty in the vertical direction than in the horizontal one [62]. Moreover, the direct model for phase measurement is especially sensitive to a vertical displacement of the reader antenna, because the UAV flies above the RFID tag [63].

Let us derive a simple model to explain the vertical sensitivity of the system. Figure 2 describes the system. As derived elsewhere [18], the phase variation $d\phi_m$ in the direct model at first order is expressed as :

$$d\phi_m = \frac{1}{\sqrt{x^2 + z^2}} \begin{bmatrix} x \\ z \end{bmatrix} [dx_r + \epsilon_x \;\; dz_r + \epsilon_z] \tag{5}$$

Where x and z are the antenna-tag distance coordinates, dx_r and dz_r are the true position variations, ϵ_x and ϵ_z are the antenna localisation errors. The GPS device that we use yields values of $\epsilon_x \approx 1$ cm and $\epsilon_z \approx 3$ cm, confirmed by the literature [64]. In usual UAV trajectories, the z coordinate is usually less prone to vary (if not set to a constant) than the horizontal coordinates. In the present step-by-step scenario, the true variation dz_r between consecutive measurements is of mm order. This implies that the modeled height variation $dz_r + \epsilon_z$ is mostly driven by the vertical error ϵ_z. In addition, the fact that $z > x$ in the general case of a drone flying over the tag, yields a higher sensitivity in the z direction. For these reasons it is important to mitigate the antenna vertical position error.

We have covered various aspects of SAR inversion, notably the choice of the cost function and the importance of the vertical tracking error. Next section will present and discuss the results.

5. Results and discussion

Before analysing the localization results, we first validate the MCMC method in comparison to a gridsearch algorithm. Then the various antenna tracking methods, and 1D localization under different media are compared. The two cost functions C_1 and C_2 are discussed, and finally 3D real-time localization is presented. In this next section, all MCMC results are presented in a statistical manner. After performing the MCMC run with a given number of candidates (typically a few 100 000), the distribution is plotted as a histogram with sub-centimeter resolution, or as a 3D scatter-plot.

5.1. Validation of MCMC localization with 1D SAR

Figure 3 presents qualitative MCMC results for a 1D-SAR experiment performed in air. The multivariate plots highlight the 3D shape of the cost function, which resembles a torus centered around the SAR axis. When projected onto Oy and Oz, the MCMC distribution indicates the presence of minor secondary peaks, although not generating localization ambiguities. An exhaustive gridsearch was computed along the main SAR directions, centered around the MCMC solution. The comparison between gridsearch and MCMC in Figure 4, shows coherent maxima. The difference in cost function shape is due to the different search spaces represented by both 3D-MCMC and 1D-gridsearch : the first represents accumulated results along the whole 3D search space, whereas the second only shows the cost function along a 1D-line. Figure 4 shows

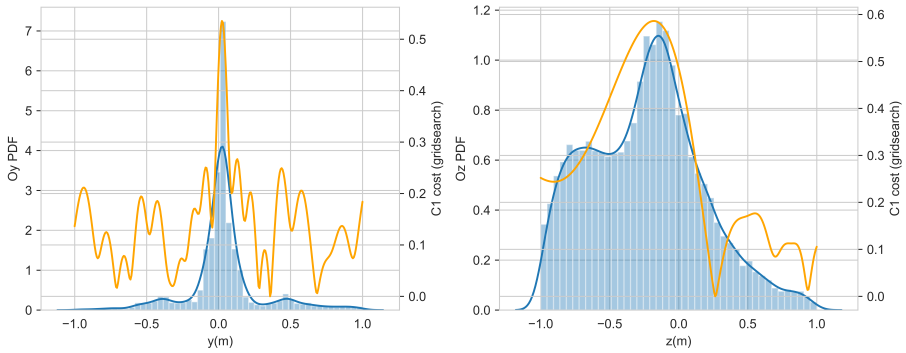

Figure 4: In blue, histogram of the MCMC distribution projected on the Oy (left) and Oz (right) axes. In orange, gridsearch estimation of the cost function along a line, centered on the estimated position.

Localization scheme	**Tacheo**	**RTK**		**PPK**
	1D	1D	Stable Z	3D
ϵ_y (cm)	< 1	1.5	1	2
ϵ_z (cm)	2.6	8	4	3

Table 2: Summary of localization results using a fiber glass stable structure, and the autonomous measurement system. The 1D experiments were performed step-by-step, while the 3D experiment was real-time.

that MCMC succeeds in accurately mapping a non-convex function for SAR-RFID phase inversion, with a lower computation time and better (virtually unlimited) resolution than a gridsearch algorithm. Moreover the MCMC output is directly exploitable for a statistical evaluation of the inversion (see below).

5.2. Tag localization using different antenna tracking methods

Table 2 shows results for 1D-localization using different antenna tracking methods. The tacheometer is the most accurate method, as could be expected from the devices' reported performance [52]. RTK and PPK yield a similar accuracy in the horizontal plane. The artificial vertical stabilization of the SAR trajectory tends to improve the vertical localization results.

Vertical stabilization for RTK. The higher vertical error for both PPK and RTK is partly induced by the poor accuracy of both methods in this direction. The reported RMS of the U-blox F9P is 3 cm in the vertical direction [65], which was also verified *in situ* during the testing phase. This Oz instability produces poor inversion results as stated previously. An artificial stabilization of the vertical coordinate was tested: a 3-point rolling average was applied on the RTK vertical coordinate, increasing the Oz localization accuracy by a factor 2 (see Table 2). This smoothing showed satisfactory results in a controlled and stabilized experiment. We believe more research should be performed in order to generalize it to real-time acquisitions. Indeed as the behavior of the SAR phase does provide information about the Oz antenna movements. A Kalman filtering approach could for example be applied in a SLAM (Simultaneous Localization and Mapping) approach, that would take into account the vertical error of the antenna as well a data fusion from IMU or Lidar devices [66, 67].

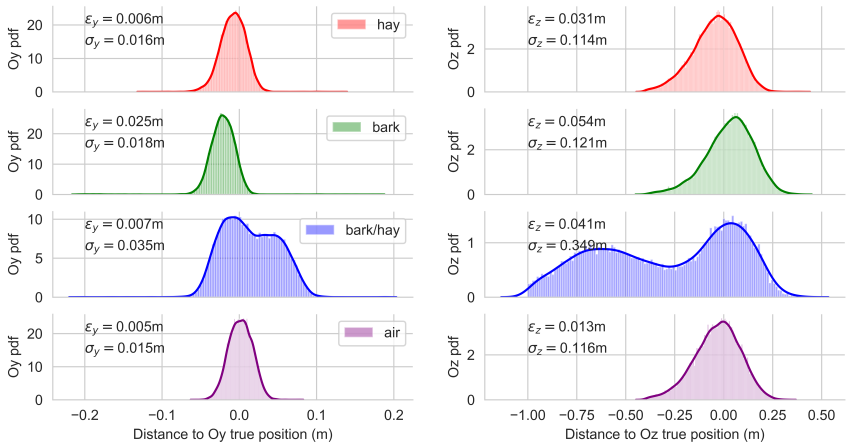

Figure 5: MCMC results for the 1D vegetation experiments, with ϵ_y and ϵ_z the localization error along Oy and Oz, σ_y and σ_z the respective standard deviation of the MCMC distribution. All results were computed using C_1.

Medium	Air	Hay	Bark	Bark/Hay	Snow C_1	Snow C_2
ϵ_y (m)	< 0.01	< 0.01	0.03	0.01	0.05	0.06
ϵ_z (m)	0.01	0.03	0.05	0.04	0.14	0.25

Table 3: Localization results for various propagation media : error ϵ_y along the 1D-SAR direction, and ϵ_z along the radial direction (or vertical).

5.3. Tag localization under vegetation and snow

The drying experiment revealed a 50% moisture content for bark, against 2% for hay. Figure 5 shows localization results for the vegetation experiments, illustrated by MCMC histograms. Hay does not show any significant effect on the radiowave time of flight, nor on the localization cost function, even when two blocks of hay are used (1m depth of material over RFID tag). As shown in Table 3, the localization error stays within centimeter margins. On the contrary, the effect of bark is more notable. The shape of the solution is not changed dramatically but the error is higher in both Oz and Oy directions. In the case of a bark/hay superposition, with the moist bark above hay, the localization results are strongly disturbed. The cost function is modified especially in the Oz direction, where a clear secondary peak appears. In both directions, the peak is widened and shows a higher deviation. This disturbance is most likely due to multipath effects, as was confirmed by comparison of phase measurements.

The localization results under snow are presented in Table 3 and Figure 6, with typical errors of about 3 cm. Using the same cost function as in the vegetation experiment (C_1), we note that the snow induces a strong secondary peak approximately one wavelength away from the main one ($\lambda \approx 16$ cm). Focusing on the main peak, a 5 cm horizontal error is still obtained, and 12 cm error in the vertical direction. The localization in air from Figure 6 shows a higher error than in the vegetation experiments, although it remains in the standard deviation limits. The cost functions will be compared below.

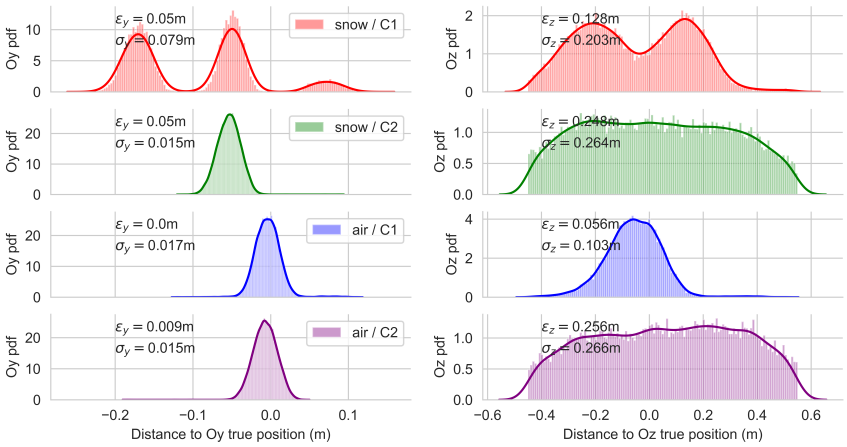

Figure 6: MCMC results for the 1D snow experiments, with a comparison between C_1 and C_2 results.

Interpretation. The sensitivity of the radiowave propagation to the bark material can be explained by its higher moisture content, as well as its mesoscale material structure, that present a high number of air/wood interfaces (RF diffraction and diffusion). Indeed, the wavelength is about 34cm and the typical bark pieces had dimension of 1-10cm. As could be expected from the mostly horizontal trajectory, the vertical direction is more sensitive to perturbations of the medium. Moreover, one specificity of the bark material was its asymmetry : one side of the bark layer was thicker, which deported the measurement bias towards a specific direction. Translated in real scenario, this highlights that non-homogeneous and moist material can strongly disturb both measurement accuracy and precision [15, 68], especially if they are elevated above ground (wet leaves for example). This is why the snow experiment was performed with dry and fresh snow : although snow can cause strong phase shifts [9], the relative homogeneity and symmetry of the medium preserved the coherence of the measurement. Nonetheless, the overall 1D results show that the effect of snow on localization are the highest compared to the tested vegetation. Besides, the snow might artificially lower the position of the tag, because of the longer optical path in snow than in air. Due to the vertical ambiguity of the results it is not possible to conclude on this aspect.

5.4. Comparison of cost functions

Figure 6 also presents MCMC results using cost functions C_1 and C_2, for the snow experiment. C_1 produces an ambiguous inversion result with multiple peaks in the presence of the snow layer. This is most likely due to the multipath interference and phase delay introduced by the snow. As a reference, we see that localization through air with C_1 yields a unique solution.

On the contrary, C_2 generates a unique optimum in both Oy and Oz directions, even in the presence of snow. This can be explained qualitatively, by stating that the guided-unwrap approach accumulates information along the whole SAR. Indeed, a correct phase unwrap is new

information for inversion and it reduces the ambiguity. We interpret C_2 as a way of averaging the phase ambiguities.
On the other hand, C_2 requires more computation time because of phase unwrapping.

Limitations of the unwrapping approach C_2. Note that the C_2 algorithm is based on the assumption that ϕ_m and ϕ_t behave in a similar way, and is built to estimate the resemblance of the two series in a real-data scenario. If the two series have nothing in common, the algorithm will produce non-realistic, over-fitting results that should be discarded. This method proves to be more stable than standard phase unwrapping, and the added information allows for a better convergence when searching for most probable tag position.

Although phase unwrapping shows considerable advantages, it is much more sensitive to perturbations. Notably when the space sampling frequency changes (UAV speed variation) and in strong weather scenarios (wind/rain/vegetation), the stability of any unwrapping algorithm is challenged [16]. Most unwrapping algorithms have been developed and tested indoors [69, 50], where the faced challenges are different (more multipathing, simpler environment). There still remains a need for outdoor validation of such algorithms.

5.5. 3D real-time localization results

Figure 7 presents MCMC results for a 3D-SAR real-time experiment using the C2 function. The localization results are provided in Table 4, with aperture length L, error ϵ between reference position and MCMC distribution average, and distribution standard deviation σ. Note that the MCMC solution error is consistently comparable to the standard deviation score (interpreted as an "error bar").

The relatively short vertical aperture explains the higher deviation in the vertical direction. This is added to the higher vertical sensitivity of the system (see Section 4.4).

Direction	Aperture length (m)	Localization error (m)	Standard deviation (m)
X	1.6	0.02	0.015
Y	1.2	0.02	0.015
Z	0.25	0.08	0.1

Table 4: Summary of the 3D-SAR localization results.

5.6. Discussion on main error directions

In the context of a mainly horizontal trajectory, the xOy and Oz estimations are often discriminated because they don't rely on the exact same inversion approach. Namely, the SAR horizontal aperture can provide a high precision in the xOy plane, whereas additional information is often needed for Oz, such as Lidar, IMU or other altitude measurement devices. Figure 7 shows qualitatively that MCMC space parameters are correlated, i.e. that the distribution is not aligned with the main axes. This challenges the horizontal/vertical separation. The strong correlation that can appear between vertical and horizontal parameters is an additional source of error. It is expected that the main error directions are not aligned with the XYZ inversion frame, and MCMC allows for a detailed analysis of these directions. Table 5 presents correlation coefficients between Oy and Oz parameters of the MCMC distribution, in the yOz plane (or perpendicular to 1D trajectory, when applicable). Note that the highest 1D scores are reached in the most RF-sensitive

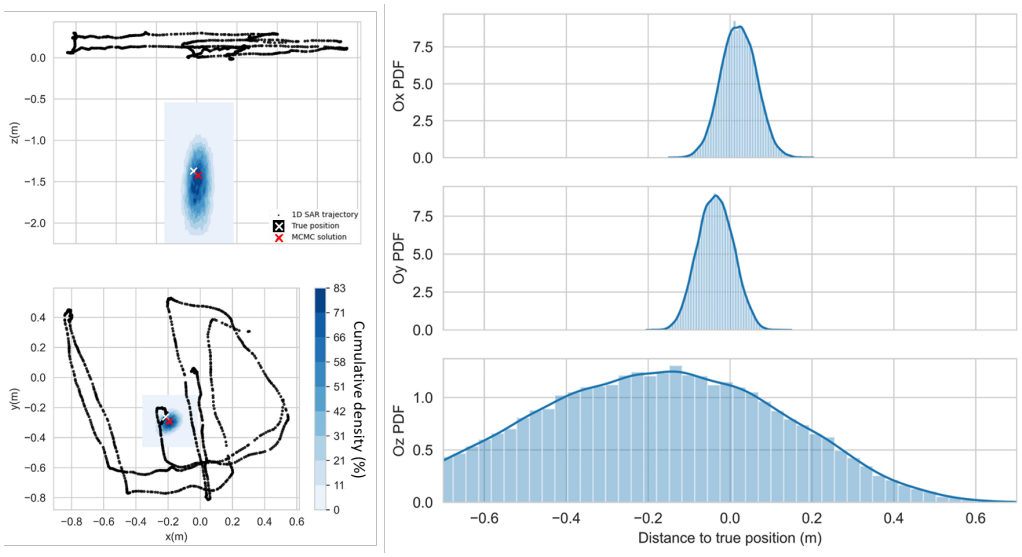

Figure 7: MCMC localization results for a tag with a 3D trajectory. (Left) 3D densities in xOy and xOz planes. (Right) MCMC density projected on every axis.

Experiment	Air	Hay	Bark	Bark/Hay	Snow	3D
yOz corr.coef	0.15	0.26	0.22	0.34	0.3	0.41

Table 5: Correlation coefficient between Oy et Oz parameters in the MCMC distribution, for various localization experiments.

media (heterogeneous and high permittivity : bark/hay and snow), indicating that multipath-rich environments also reshape the cost function's main directions. The higher correlation in the 3D case is also an effect of the trajectory, which is not symmetrical nor uniformly sampled. This highlights the necessity to identify eigenvectors of the MCMC distribution and compare them to the usual horizontal-vertical directions.

6. Conclusion and perspectives

This paper presents various advances aiming towards centimeter localization with SAR-RFID devices, in outdoor conditions. The feasibility of localization under vegetation and snow cover was demonstrated, and limitations concerning moisture content and medium homogeneity were highlighted. Localization errors under vegetation do not exceed 5 cm in the vertical direction, and 1 cm in the horizontal plane. Under snow, the vertical localization error was about 10 cm, and 4 cm in the horizontal plane. Two cost functions were compared for SAR inversion, highlighting that guided phase unwrapping resolves ambiguities, but lowers the vertical precision. Three antenna tracking methods were compared, namely tacheometry / RTK / PPK and showed that PPK was best suited for landslide monitoring purposes. An optimization algorithm based on Markov-Chain Monte Carlo was employed for inversion, providing both high accuracy and estimation of parameter covariance. Real-time measurements performed with a handheld SAR-RFID structure, demonstrated centimeter accuracy and precision in the horizontal plane. As expected the

vertical accuracy of SAR-RFID is the lowest and most sensitive to multipath interference from the propagation environment. Various solutions to this issue could be for example : a diversified trajectory lowering the sensitivity to vertical direction, or the use of a lidar or accelerometer to provide a more stable vertical position.
This study of SAR-RFID systems suggests interesting perspectives of improvement, notably by improving antenna positioning using for example GPS-IMU fusion, and of course real UAV monitoring on landslides. As a side-use, this method could also be used for material sensing by exploiting the RF disturbance of snow or vegetation. SAR-RFID approach is promising for landslide surface monitoring. More experiments are needed in vegetated and snowy environments, especially in humid scenarios. UAV measurements showed that research efforts should be dedicated to estimate and correct the lever-arm effect from GNSS rover to antenna center.

7. Aknowledgements

The authors would like to thank the Géolithe company for its implication in the project, notably concerning equipment and software. In particular we would like to thank Nicolas Grunbaum for his dedication in the early stages of the project.

8. Funding

This work was partially funded by the Region Auvergne Rhone Alpes through the Pacte de Recherche LABCOM GEO3ILAB and the RISQID projects, along with contribution from Géolithe. This work is part of the “Habitability” LABEX coordinated by OSUG.

References

[1] N. Mohd Noor, A. Abdullah, M. Hashim, Remote sensing uav/drones and its applications for urban areas: A review, in: IOP conference series: Earth and environmental science, Vol. 169, IOP Publishing, 2018, p. 012003.
[2] C. H. Hugenholtz, B. J. Moorman, K. Riddell, K. Whitehead, Small unmanned aircraft systems for remote sensing and earth science research, Eos, Transactions American Geophysical Union 93 (25) (2012) 236–236.
[3] U. Niethammer, M. James, S. Rothmund, J. Travelletti, M. Joswig, Uav-based remote sensing of the super-sauze landslide: Evaluation and results, Engineering Geology 128 (2012) 2–11.
[4] M. Peppa, J. Mills, P. Moore, P. Miller, J. Chambers, Accuracy assessment of a uav-based landslide monitoring system, The international archives of the photogrammetry, remote sensing and spatial information sciences 41 (2016) 895–902.
[5] W. Feng, J. Wang, Y. Chen, X. Wang, N. Ge, J. Lu, Uav-aided mimo communications for 5g internet of things, IEEE Internet of Things Journal 6 (2) (2018) 1731–1740.
[6] A. D. Boursianis, M. S. Papadopoulou, P. Diamantoulakis, A. Liopa-Tsakalidi, P. Barouchas, G. Salahas, G. Karagiannidis, S. Wan, S. K. Goudos, Internet of things (iot) and agricultural unmanned aerial vehicles (uavs) in smart farming: A comprehensive review, Internet of Things 18 (2022) 100187.
[7] X. Jia, Q. Feng, T. Fan, Q. Lei, Rfid technology and its applications in internet of things (iot), in: 2012 2nd international conference on consumer electronics, communications and networks (CECNet), IEEE, 2012, pp. 1282–1285.
[8] M. Le Breton, L. Baillet, E. Larose, E. Rey, P. Benech, D. Jongmans, F. Guyoton, M. Jaboyedoff, Passive radio-frequency identification ranging, a dense and weather-robust technique for landslide displacement monitoring, Engineering geology 250 (2019) 1–10.
[9] M. Le Breton, É. Larose, L. Baillet, Y. Lejeune, A. van Herwijnen, Monitoring snow water equivalent using the phase of rfid signals, The Cryosphere 17 (8) (2023) 3137–3156.
[10] A. Motroni, P. Nepa, Uav-based 3d localization of passive uhf-rfid tags empowering outdoor stock management.
[11] M. Cassel, H. Piégay, G. Fantino, J. Lejot, L. Bultingaire, K. Michel, F. Perret, Comparison of ground-based and uav a-uhf artificial tracer mobility monitoring methods on a braided river, Earth Surface Processes and Landforms 45 (5) (2020) 1123–1140.

[12] H. Piégay, F. Arnaud, B. Belletti, M. Bertrand, S. Bizzi, P. Carbonneau, S. Dufour, F. Liébault, V. Ruiz-Villanueva, L. Slater, Remotely sensed rivers in the anthropocene: State of the art and prospects, Earth Surface Processes and Landforms 45 (1) (2020) 157–188.
[13] V. Ilinca, I. Șandric, Z. Chițu, R. Irimia, I. Gheuca, Uav applications to assess short-term dynamics of slow-moving landslides under dense forest cover, Landslides 19 (7) (2022) 1717–1734.
[14] B.-G. Chae, H.-J. Park, F. Catani, A. Simoni, M. Berti, Landslide prediction, monitoring and early warning: a concise review of state-of-the-art, Geosciences Journal 21 (2017) 1033–1070.
[15] M. Le Breton, L. Baillet, E. Larose, E. Rey, P. Benech, D. Jongmans, F. Guyoton, Outdoor uhf rfid: Phase stabilization for real-world applications, IEEE Journal of Radio Frequency Identification 1 (4) (2017) 279–290.
[16] A. Charléty, M. Le Breton, L. Baillet, E. Larose, Long-term monitoring of soil surface deformation with rfid, in: 2022 IEEE 12th International Conference on RFID Technology and Applications (RFID-TA), IEEE, 2022, pp. 101–104.
[17] A. Charléty, M. Le Breton, L. Baillet, E. Larose, Rfid landslide monitoring: long-term outdoor signal processing and phase unwrapping, IEEE Journal of Radio Frequency Identification (2023).
[18] A. Charléty, M. Le Breton, E. Larose, L. Baillet, 2d phase-based rfid localization for on-site landslide monitoring, Remote Sensing 14 (15) (2022) 3577.
[19] M. Le Breton, L. Baillet, E. Larose, Tomography of the quantity of grass using rfid propagation-based sensing (2023).
[20] M. Le Breton, F. Liébault, L. Baillet, A. Charléty, É. Larose, S. Tedjini, Dense and long-term monitoring of earth surface processes with passive rfid—a review, Earth-Science Reviews (2022) 104225.
[21] R. M. Alkan, S. Erol, I. M. Ozulu, V. Ilci, Accuracy comparison of post-processed ppp and real-time absolute positioning techniques, Geomatics, Natural Hazards and Risk 11 (1) (2020) 178–190.
[22] J. F. G. Monico, H. A. Marques, Í. Tsuchiya, R. T. Oyama, W. R. S. d. Queiroz, M. C. d. Souza, J. P. Wentz, Real time ppp applied to airplane fligtht tests, Boletim de Ciências Geodésicas 25 (2019).
[23] E. Remzi, E. Alkan, A. AYDIN, A comparative analysis of uav-rtk and uav-ppk methods in mapping different surface types, European Journal of Forest Engineering 7 (1) (2020) 12–25.
[24] T. Suzuki, Y. Takahashi, Y. Amano, Precise uav position and attitude estimation by multiple gnss receivers for 3d mapping, in: Proceedings of the 29th International Technical Meeting of the Satellite Division of The Institute of Navigation (ION GNSS+ 2016), 2016, pp. 1455–1464.
[25] D. Janos, P. Kuras, Ł. Ortyl, Evaluation of low-cost rtk gnss receiver in motion under demanding conditions, Measurement 201 (2022) 111647.
[26] M. Daakir, M. Pierrot-Deseilligny, P. Bosser, F. Pichard, C. Thom, Y. Rabot, Study of lever-arm effect using embedded photogrammetry and on-board gps receiver on uav for metrological mapping purpose and proposal of a free ground measurements calibration procedure, The International Archives of the Photogrammetry, Remote Sensing and Spatial Information Sciences 40 (2016) 65–70.
[27] C. Li, E. Tanghe, P. Suanet, D. Plets, J. Hoebeke, E. De Poorter, W. Joseph, Reloc 2.0: Uhf-rfid relative localization for drone-based inventory management, IEEE Transactions on Instrumentation and Measurement 70 (2021) 1–13.
[28] A. Buffi, A. Motroni, P. Nepa, B. Tellini, R. Cioni, A sar-based measurement method for passive-tag positioning with a flying uhf-rfid reader, IEEE Transactions on Instrumentation and Measurement 68 (3) (2018) 845–853.
[29] F. Bernardini, A. Buffi, D. Fontanelli, D. Macii, V. Magnago, M. Marracci, A. Motroni, P. Nepa, B. Tellini, Robot-based indoor positioning of uhf-rfid tags: The sar method with multiple trajectories, IEEE Transactions on Instrumentation and Measurement 70 (2020) 1–15.
[30] F. Bernardini, A. Buffi, A. Motroni, P. Nepa, B. Tellini, P. Tripicchio, M. Unetti, Particle swarm optimization in sar-based method enabling real-time 3d positioning of uhf-rfid tags, IEEE Journal of Radio Frequency Identification 4 (4) (2020) 300–313.
[31] A. Tzitzis, A. R. Chatzistefanou, T. V. Yioultsis, A. G. Dimitriou, A real-time multi-antenna sar-based method for 3d localization of rfid tags by a moving robot, IEEE Journal of Radio Frequency Identification 5 (2) (2021) 207–221.
[32] S. Bisnath, D. Wells, M. Santos, K. Cove, Initial results from a long baseline, kinematic, differential gps carrier phase experiment in a marine environment, in: PLANS 2004. Position Location and Navigation Symposium (IEEE Cat. No. 04CH37556), IEEE, 2004, pp. 625–631.
[33] J. Jackson, B. Davis, D. Gebre-Egziabher, A performance assessment of low-cost rtk gnss receivers, in: 2018 IEEE/ION Position, Location and Navigation Symposium (PLANS), IEEE, 2018, pp. 642–649.
[34] K. Maciuk, Gps-only, glonass-only and combined gps+ glonass absolute positioning under different sky view conditions, Tehnički vjesnik 25 (3) (2018) 933–939.
[35] E. Cledat, L. V. Jospin, D. A. Cucci, J. Skaloud, Mapping quality prediction for rtk/ppk-equipped micro-drones operating in complex natural environment, ISPRS Journal of Photogrammetry and Remote Sensing 167 (2020) 24–38.
[36] D. Gautam, A. Lucieer, C. Watson, C. McCoull, Lever-arm and boresight correction, and field of view determi-

nation of a spectroradiometer mounted on an unmanned aircraft system, ISPRS Journal of Photogrammetry and Remote Sensing 155 (2019) 25–36.
[37] M. Zhong, Q. Cao, J. Guo, D. Zhou, Simultaneous lever-arm compensation and disturbance attenuation of pos for a uav surveying system, IEEE Transactions on Instrumentation and Measurement 65 (12) (2016) 2828–2839.
[38] C. V. Angelino, V. R. Baraniello, L. Cicala, Uav position and attitude estimation using imu, gnss and camera, in: 2012 15th International Conference on Information Fusion, IEEE, 2012, pp. 735–742.
[39] W. You, F. Li, L. Liao, M. Huang, Data fusion of uwb and imu based on unscented kalman filter for indoor localization of quadrotor uav, Ieee Access 8 (2020) 64971–64981.
[40] C. Eling, M. Wieland, C. Hess, L. Klingbeil, H. Kuhlmann, Development and evaluation of a uav based mapping system for remote sensing and surveying applications, The International Archives of the Photogrammetry, Remote Sensing and Spatial Information Sciences 40 (2015) 233–239.
[41] K. F. Hasan, Y. Feng, Y.-C. Tian, Gnss time synchronization in vehicular ad-hoc networks: Benefits and feasibility, IEEE Transactions on Intelligent Transportation Systems 19 (12) (2018) 3915–3924.
[42] S.-F. Ch'ng, A. Khosravian, A.-D. Doan, T.-J. Chin, Outlier-robust manifold pre-integration for ins/gps fusion, in: 2019 IEEE/RSJ International Conference on Intelligent Robots and Systems (IROS), IEEE, 2019, pp. 7489–7496.
[43] S. Lu, C. Xu, R. Y. Zhong, An active rfid tag-enabled locating approach with multipath effect elimination in agv, IEEE Transactions on Automation Science and Engineering 13 (3) (2016) 1333–1342.
[44] G. Wang, C. Qian, K. Cui, X. Shi, H. Ding, W. Xi, J. Zhao, J. Han, A universal method to combat multipaths for rfid sensing, in: IEEE INFOCOM 2020-IEEE Conference on Computer Communications, IEEE, 2020, pp. 277–286.
[45] G. Casati, M. Longhi, D. Latini, F. Carbone, S. Amendola, F. Del Frate, G. Schiavon, G. Marrocco, The interrogation footprint of rfid-uav: Electromagnetic modeling and experimentations, IEEE Journal of Radio Frequency Identification 1 (2) (2017) 155–162.
[46] D. A. Tesch, E. L. Berz, F. P. Hessel, Rfid indoor localization based on doppler effect, in: Sixteenth International Symposium on Quality Electronic Design, IEEE, 2015, pp. 556–560.
[47] A. Azarfar, N. Barbot, E. Perret, Chipless rfid based on micro-doppler effect, IEEE Transactions on Microwave Theory and Techniques 70 (1) (2021) 766–778.
[48] C. E. Shannon, Communication in the presence of noise, Proceedings of the IRE 37 (1) (1949) 10–21.
[49] Y. Ma, H. Liu, Y. Zhang, Y. Jiang, The influence of the nonideal phase offset on sar-based localization in passive uhf rfid, IEEE Transactions on Antennas and Propagation 68 (8) (2020) 6346–6354.
[50] A. Tzitzis, S. Megalou, S. Siachalou, T. G. Emmanouil, A. Kehagias, T. V. Yioultsis, A. G. Dimitriou, Localization of rfid tags by a moving robot, via phase unwrapping and non-linear optimization, IEEE Journal of Radio Frequency Identification 3 (4) (2019) 216–226.
[51] M. García-Fernández, Y. Álvarez López, A. De Mitri, D. Castrillo Martínez, G. Álvarez-Narciandi, F. Las-Heras Andrés, Portable and easily-deployable air-launched gpr scanner, Remote Sensing 12 (11) (2020) 1833.
[52] M. Bláha, H. Eisenbeiss, D. Grimm, P. Limpach, Direct georeferencing of uavs, The International Archives of the Photogrammetry, Remote Sensing and Spatial Information Sciences 38 (2012) 131–136.
[53] T. Takasu, A. Yasuda, Development of the low-cost rtk-gps receiver with an open source program package rtklib, in: International symposium on GPS/GNSS, Vol. 1, International Convention Center Jeju Korea Seogwipo-si, Republic of Korea, 2009, pp. 1–6.
[54] Mayer Analytics. pyUBX https://github.com/mayeranalytics/pyUBX.
[55] S. Sarkka, V. V. Viikari, M. Huusko, K. Jaakkola, Phase-based uhf rfid tracking with nonlinear kalman filtering and smoothing, IEEE Sensors Journal 12 (5) (2011) 904–910.
[56] L. M. Ni, Y. Liu, Y. C. Lau, A. P. Patil, Landmarc: Indoor location sensing using active rfid, in: Proceedings of the First IEEE International Conference on Pervasive Computing and Communications, 2003.(PerCom 2003)., IEEE, 2003, pp. 407–415.
[57] K. Han, S. H. Cho, Advanced landmarc with adaptive k-nearest algorithm for rfid location system, in: 2010 2nd IEEE InternationalConference on Network Infrastructure and Digital Content, IEEE, 2010, pp. 595–598.
[58] W. R. Gilks, S. Richardson, D. Spiegelhalter, Markov chain Monte Carlo in practice, CRC press, 1995.
[59] A. Serripierri, L. Moreau, P. Boue, J. Weiss, P. Roux, Recovering and monitoring the thickness, density, and elastic properties of sea ice from seismic noise recorded in svalbard, The Cryosphere 16 (6) (2022) 2527–2543.
[60] L. Moreau, A. J. Hunter, A. Velichko, P. D. Wilcox, 3-d reconstruction of sub-wavelength scatterers from the measurement of scattered fields in elastic waveguides, IEEE transactions on ultrasonics, ferroelectrics, and frequency control 61 (11) (2014) 1864–1879.
[61] K.-L. Du, M. Swamy, K.-L. Du, M. Swamy, Simulated annealing, Search and Optimization by Metaheuristics: Techniques and Algorithms Inspired by Nature (2016) 29–36.
[62] P. A. Zandbergen, S. J. Barbeau, Positional accuracy of assisted gps data from high-sensitivity gps-enabled mobile phones, The Journal of Navigation 64 (3) (2011) 381–399.
[63] G. Bandini, A. Motroni, A. Buffi, M. Marracci, B. Tellini, On the effect of position uncertainty of the uhf-rfid reader trajectory in sar-based localization via uav, in: 2022 IEEE International Symposium on Measurements &

Networking (M&N), IEEE, 2022, pp. 1–6.
[64] D. Janos, P. Kuras, Evaluation of low-cost gnss receiver under demanding conditions in rtk network mode, Sensors 21 (16) (2021) 5552.
[65] U. Robustelli, M. Cutugno, G. Pugliano, Low-cost gnss and ppp-rtk: Investigating the capabilities of the u-blox zed-f9p module, Sensors 23 (13) (2023) 6074.
[66] A. Gupta, X. Fernando, Simultaneous localization and mapping (slam) and data fusion in unmanned aerial vehicles: Recent advances and challenges, Drones 6 (4) (2022) 85.
[67] A. Charléty, O. J. Michel, M. Le Breton, Kalman smoothing for better rfid landslide monitoring, in: 2023 31st European Signal Processing Conference (EUSIPCO), IEEE, 2023, pp. 1679–1682.
[68] S. F. Pichorim, N. J. Gomes, J. C. Batchelor, Two solutions of soil moisture sensing with rfid for landslide monitoring, Sensors 18 (2) (2018) 452.
[69] P. Tripicchio, M. Unetti, S. D'Avella, A. Buffi, A. Motroni, F. Bernardini, P. Nepa, A synthetic aperture uhf rfid localization method by phase unwrapping and hyperbolic intersection, IEEE Transactions on Automation Science and Engineering 19 (2) (2021) 933–945.